

Effect of Hydrogen and Helium on Irradiation Damage Accumulation in Nickel

September 2024

G. Nandipati D. J. Edwards A. Roy D. J. Senior A. M. Casella

DISCLAIMER

This report was prepared as an account of work sponsored by an agency of the United States Government. Neither the United States Government nor any agency thereof, nor Battelle Memorial Institute, nor any of their employees, makes **any warranty, express or implied, or assumes any legal liability or responsibility for the accuracy, completeness, or usefulness of any information, apparatus, product, or process disclosed, or represents that its use would not infringe privately owned rights.** Reference herein to any specific commercial product, process, or service by trade name, trademark, manufacturer, or otherwise does not necessarily constitute or imply its endorsement, recommendation, or favoring by the United States Government or any agency thereof, or Battelle Memorial Institute. The views and opinions of authors expressed herein do not necessarily state or reflect those of the United States Government or any agency thereof.

PACIFIC NORTHWEST NATIONAL LABORATORY
operated by
BATTELLE
for the
UNITED STATES DEPARTMENT OF ENERGY
under Contract DE-AC05-76RL01830

Printed in the United States of America

Available to DOE and DOE contractors from
the Office of Scientific and Technical Information,
P.O. Box 62, Oak Ridge, TN 37831-0062

www.osti.gov

ph: (865) 576-8401

fox: (865) 576-5728

email: reports@osti.gov

Available to the public from the National Technical Information Service
5301 Shawnee Rd., Alexandria, VA 22312

ph: (800) 553-NTIS (6847)

or (703) 605-6000

email: info@ntis.gov

Online ordering: <http://www.ntis.gov>

Effect of Hydrogen and Helium on Irradiation Damage Accumulation in Nickel

September 2024

G. Nandipati D. J. Edwards A. Roy D. J. Senior A. M. Casella

Prepared for
the U.S. Department of Energy
Under Contract DE-AC05-76RL01830

Pacific Northwest National Laboratory
Richland, Washington 99354

Abstract

We report our results on the study of the effects of hydrogen and helium on irradiation damage accumulation in nickel, aiming to understand the TEM observations made by Edwards et al. regarding the Ni-coatings protecting the getter tube in a TPBAR. We hypothesized that differences in the fluxes of ^3H and/or He between the coatings might explain these microstructural variations. However, our simulation results show that during the initial stages of irradiation, the presence of H or He enhances void nucleation by stabilizing small vacancy clusters against thermal dissociation and does not enhance void growth. Nevertheless, we think that helium's higher diffusivity, stronger binding with vacancy clusters, and ability to displace a nearby lattice atom—either to create a new vacancy or to enlarge an existing vacancy cluster—could result in a larger average vacancy cluster size. Therefore, it is likely that void growth will occur post-nucleation phase as more He accumulates at higher doses than those simulated in this study.

Acronyms and Abbreviations

1D	One-Dimensional
2D	Two-Dimensional
3D	Three-Dimensional
Al	Aluminum
BKL	Bortz-Kalos-Liebowitz
DPA	Displacements Per Atom
FCC	Face-Centered Cubic
Fe	Iron
H	Hydrogen/Protium
H ⁺	Hydrogen Ion
HCP	Hexagonal Close Packed
He	Helium
He ⁺	Helium Ion
HFIR	High-Flux Isotope Reactor
KMC	Kinetic Monte Carlo
KSOME	Kinetic Simulations of Microstructural Evolution
MD	Molecular Dynamics
Ni	Nickel
Ni ⁺	Nickel ion
NRT	Norgett-Robinson-Torrens
OKMC	Object Kinetic Monte Carlo
PKA	Primary Knock-on Atom
PNNL	Pacific Northwest National Laboratory
PWR	Pressurized Water Reactor
SIA	Self-Interstitial Atom
TEM	Transmission Electron Microscope
TPBAR	Tritium-Producing Burnable Absorber Rods
TPP	Tritium Technology Program
³ H	Tritium

Acknowledgments

This work was funded by the National Nuclear Security Administration (NNSA) of the US Department of Energy (DOE) through the Tritium Technology Program at Pacific Northwest National Laboratory. This research was carried out using institutional computing resources at Pacific Northwest National Laboratory. PNNL is a multiprogram national laboratory operated by Battelle Memorial Institute for the US DOE under DE-AC06-76RLO 1830.

Contents

Abstract	iv
Acronyms and Abbreviations	v
Acknowledgments	vi
1.0 Introduction	1
2.0 Simulation Details	3
2.1 Object Kinetic Monte Carlo Method	3
2.2 Primary Damage and PKA Spectrum	4
2.3 Simulation Cell	5
2.4 Diffusion & Reactions of Defects	5
2.4.1 Diffusion & Reaction of Vacancy Clusters	5
2.4.2 Diffusion & Reaction of SIA Clusters	6
2.4.3 Diffusion of H and He in Ni	6
2.4.3.1 Helium	6
2.4.3.2 Hydrogen	7
2.4.4 H and He and their interaction with SIAs and Vacancies	7
2.4.4.1 Hydrogen	7
2.4.4.2 Helium	8
3.0 Results and Discussions	9
3.1 Without H and He	9
3.2 With H	10
3.3 With He	13
4.0 Summary	14
5.0 References	16

Figures

1	Schematic diagram of the TPBAR showing the Ni-plated Zircaloy-4 getter	1
2	TEM Images showing voids in inner(top) and outer(bottom) Ni-coatings	2
3	Schematic diagram showing the execution of radiation damage simulation using the OKMC method.	3
4	PKA spectra (N° of recoils per unit energy) Vs. the recoil atoms' energy T in pure ^{58}Ni (green) and normalized probability density (spectral density) of a PKA Vs. recoil energy(red)	4
5	Density of vacancies	9
6	Density of Vacancy clusters	9
7	Average vacancy cluster sizes (N° of vacancies)	9
8	Total density of vacancies	11
9	Total density V and HV clusters	11
10	Combined average N° of vacancies in V and HV	11
11	Vacancy density in pure vacancy clusters	11
12	Pure vacancy cluster density	11
13	Average N° of vacancies per cluster	11
14	Total density of vacancies	12
15	Total density V and HeV clusters	12
16	Combined average N° vacancies in V and HeV	12

Tables

1	Activation energy barriers (E_a), binding energies (E_b) and detrapping barriers (E_d) of vacancy clusters. E_d is a sum of binding energy and activation energy barrier for single vacancy. D_0 is the diffusion prefactor.	6
2	Activation energies and the corresponding prefactors for SIA cluster diffusion	6
3	Activation energies and the corresponding prefactors for He cluster diffusion	7
4	Activation energies and the corresponding prefactors H_nV cluster diffusion diffusion	8
5	Detrapping barrier and prefactors used for the dissociation of HeI , He_2I and HeI_2 clusters	8

1.0 Introduction

The TPBARs used in the US DOE's Tritium Readiness Program are designed to produce ^3H in commercial PWR fuel assemblies [1, 2]. As illustrated in Fig. 1, the TPBAR comprises a Zircaloy-4 getter tube located between the cladding and the LiAlO_2 pellets [1, 2]. The Zircaloy-4 getter is sandwiched between Ni-plating to prevent the oxidation of its surface, which would reduce the absorption rate of ^3H that is diffusing outwards from LiAlO_2 pellets and prevent it from reaching the cladding. Therefore, the integrity of Ni-plating is crucial to protect the Zircaloy-4 getter for oxidation, thereby inhibiting/preventing the escape of ^3H into reactor coolant and, in turn, into the environment. The Ni-plating is subjected to neutron irradiation, permeation of ^3H produced from the pellets, and the production of H and He due to the transmutation of Ni during irradiation [3] as well as He from tritium decay ($^3\text{H} \rightarrow ^3\text{He}$). Numerous studies in Ni and other metals have shown that He promotes/enhances void swelling. At the same time, there is a vast literature on H-induced embrittlement of Ni and other metals. Hence, understanding the microstructural changes in nickel under reactor conditions is critical, particularly as a TPBAR component, considering the vital role of Ni in protecting the getter tube.

In a previous TTP Science project, Edwards *et al.* [4] reported that voids and cavities formed in both the exterior and interior Ni coatings on the Zircaloy-4 getter tube at the mid-plane section as shown in Fig. 2. The area where the Ni and getter meet also showed cracking and porosity, possibly due in part to the accumulation of He during irradiation. This swelling could weaken the structural stability of the Ni coating and impede the transport of tritium to the getter, as the voids could potentially store ^3H . Edwards *et al.* noted that both sides had a similar number density of cavities (about $10^{21}/\text{m}^3$) at the interface with the zirconium getter. However, the distribution of cavities in the interior coating was observed to skew towards larger sizes than the outer coating, resulting in the internal Ni coating swelling 10 times more than the external coating. It was suggested that this difference could be due to different ^3H fluxes (and subsequent He from its decay) at the two coatings, with competing fluxes from the equilibrium ^3H pressure between the getter and the Fe-Al coating versus the tritium diffusing from the adjacent Zircaloy-4 getter into the Ni coating. On the pellet side, the competing fluxes arise from the back diffusion of ^3H from the getter versus the ^3H produced directly by the pellets. These factors might lead to cavities forming at similar rates in the early stages of irradiation but exhibiting different growth rates as the dose increases. The present study aims to elucidate the reasons behind the difference in void swelling between the inner and outer Ni coatings, as well as the distribution of accumulated He in the coating layers and interfaces, which is crucial for comprehending the impact of variations in irradiation conditions on radiation damage accumulation. Particularly how the damage-microstructure evolves during irradiation in the presence of H and He in Ni.

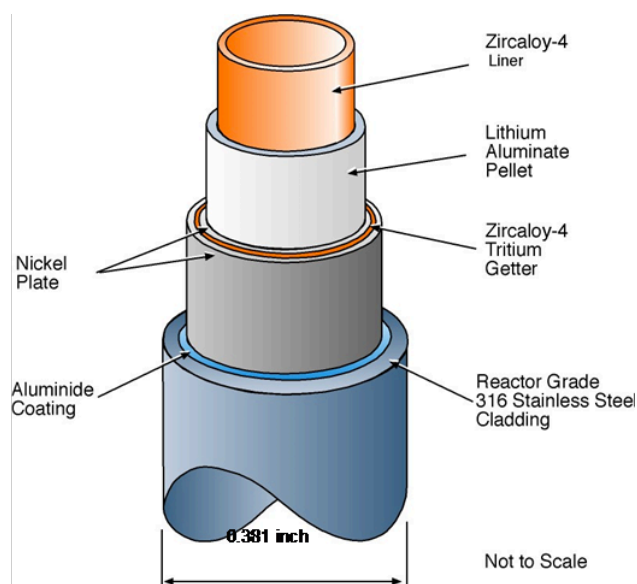


Figure 1: Schematic diagram of the TPBAR showing the Ni-plated Zircaloy-4 getter

In this report, we present our results from our modeling study of the damage accumulation in Ni under neutron irradiation using KSOME [5–7], an OKMC tool developed at PNNL to study the irradiation microstructure evolution [8, 9]. We conducted simulations of radiation damage accumulation in Ni at different H and He production rates to understand how defect microstructure evolves, particularly the density, average size, and size distribution of the voids, as well as void swelling at a dose rate comparable to commercial nuclear reactors (10^{-6} – 10^{-7} dpa/s) using an extensive cascade database generated using MD simulations [10]. Furthermore, the present study incorporates most of the available knowledge on the defect-reaction kinetics in Ni, such as those between H & vacancy, He & vacancy, H & SIA and He & SIA type defect clusters.

This report is organized as follows: Section 2.0 provides detailed simulation information. Section 2.1 describes the Object Kinetic Monte Carlo (OKMC) method and briefly explains how it is used to model radiation damage accumulation. Details on the PKA spectrum are provided in Section 2.2. The simulation cell and boundary conditions employed are discussed in Section 2.3, and the diffusion-reaction energetics of defects are detailed in Section 2.4. Our results are presented in Section 3.0, and we summarize our findings in Section 4.0.

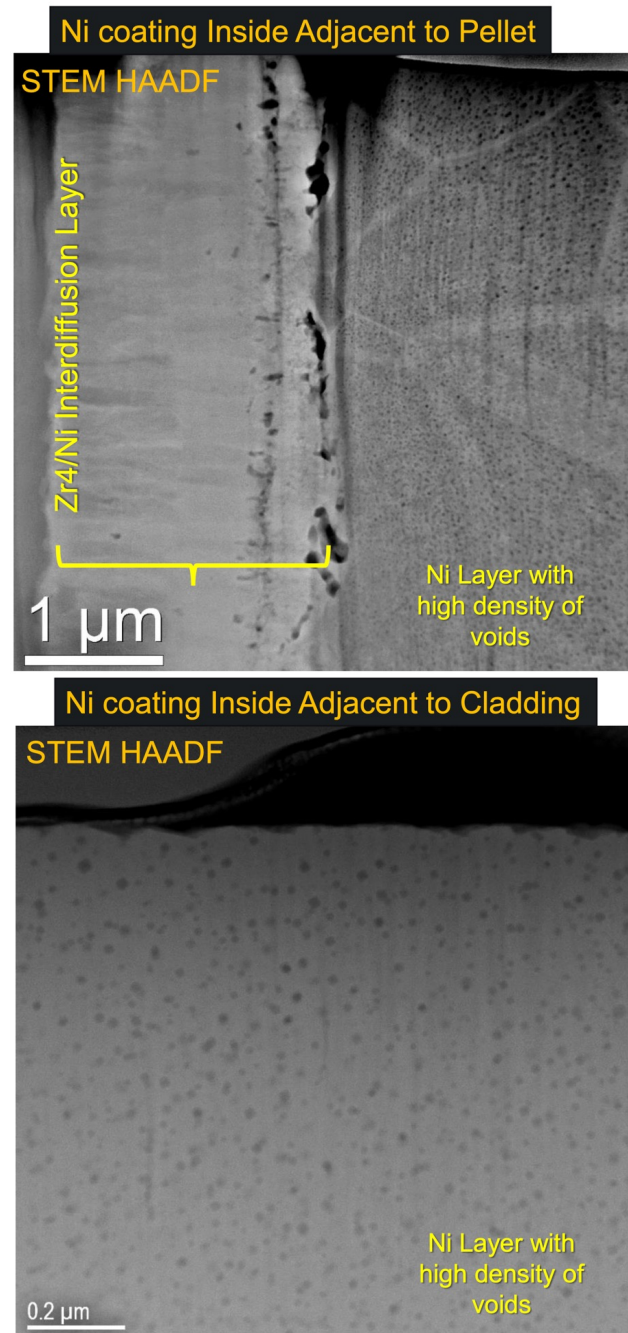


Figure 2: TEM Images showing voids in inner(top) and outer(bottom) Ni-coatings

2.0 Simulation Details

2.1 Object Kinetic Monte Carlo Method

In the OKMC method, an object can be an individual atom or clusters of atoms or an individual point defect or point defect cluster. For an irradiation damage simulation, the objects of interest include vacancies, SIAs, interstitial impurities, and their respective clusters produced during irradiation. Depending on the properties of these defects, the events these objects can perform include diffusion, dissolution (emission of defects from a cluster), and transformation of defect conformation and diffusion types. The probabilities for these events are calculated in terms of Arrhenius frequencies for thermally activated events, $R_i = \nu_i \exp(-E_i/k_B T)$. The interaction between two objects is treated as a non-activated or spontaneous event. Note that an object can range from a single atom to as large as a defect cluster, and at a minimum, every object is defined by its location, defect type, and size. Apart from standard properties, one can assign additional properties to a defect if such information is available. For example, one can differentiate between glissile and sessile SIA clusters or between a vacancy loop and a spherical void.

Defects and defect clusters, based on their properties, can diffuse in 1-, 2-, or 3-dimensions. Clusters can emit one or more defects; for instance, a vacancy (V), self-interstitial atom (SIA), or interstitial impurity atom (IIA) can release single or multiple entities of the same type. Complexes such as V+IIA or SIA+IIA might emit basic units or more complex forms. Emission events may include loop punching or trap mutation. Besides migration and emission, defects can undergo transformation events, such as rotations, directional changes in 1D diffusing SIA clusters, or transformations of a vacancy loop into a spherical void or from a glissile to a sessile loop.

When two defects come within a specific interaction distance, a non-thermally activated "reaction event" occurs. A reaction event could be the annihilation of defects (for example, a self-interstitial atom meeting a vacancy) or the aggregation of a point defect to form a cluster. These reaction events are diffusion-limited and spontaneous, and do not affect the simulation time. We identify these events by checking if defect clusters are closer to each other than their combined capture radii. Once identified, these events are executed immediately. All possible reaction events are executed before proceeding with the next KMC step.

KSOME is a computationally efficient object kinetic Monte Carlo (OKMC) code [5] to simulate microstructural evolution under irradiation over long time scales. It is named after ALSOME [11], developed at PNNL in

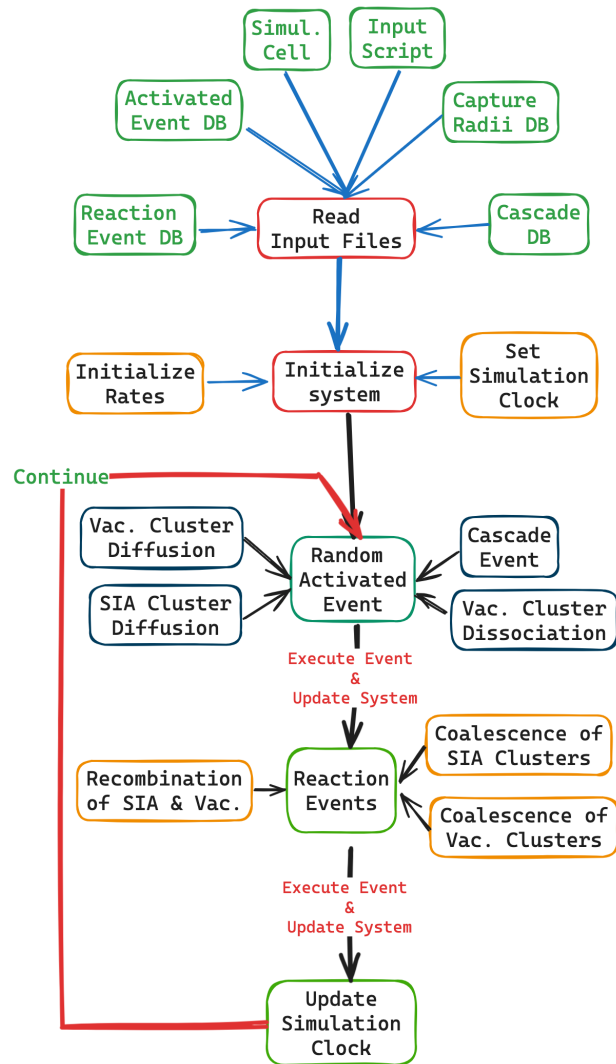


Figure 3: Schematic diagram showing the execution of radiation damage simulation using the OKMC method.

the early 80s for a similar purpose. However, KSOME is significantly more sophisticated, faster, and flexible. KSOME utilizes a rejection-free kMC algorithm, specifically the BKL method [12], and enhances simulation efficiency through a binary tree algorithm combined with lists [13]. The system selects events randomly, weighted by their rate, and updates the simulation clock using an exponential distribution for time increments.

The flow chart shown in Fig. 3 illustrates the simulation process for modeling radiation damage in materials using the object kinetic Monte Carlo (OKMC) method. This flow chart represents the iterative process of simulating radiation damage. It involves a sequence of random events executed in a time-dependent manner. The state of the system is dynamic and is continuously updated based on events such as diffusion, cluster reactions, coalescence, or recombination of defects after each primary damage event resulting from neutron-atom collision. This continuous update of the dynamic state allows modeling the long-term evolution of radiation damage in materials. It's important to note that Fig. 3 is a schematic representation when only the vacancy- and SIA-type defects are produced due to cascade damage.

The simulation begins by reading input files, including the simulation cell, input script, and several databases that contain information about activated events, capture radii, cascades, and reaction events. Once input is processed, the system is initialized based on the simulation conditions, such as the rates of diffusion and reactions, and the simulation clock is set to track the time-dependent evolution of radiation damage. The simulation then selects a random event to execute from possible events like vacancy and SIA (self-interstitial atom) cluster diffusion, vacancy dissociation, displacement cascades, coalescence of clusters, and recombination of defects. After executing the chosen event, the system is updated to reflect changes such as defect movement, recombination, or coalescence, and the simulation clock is advanced. This process of selecting, executing, and updating events continues iteratively until the simulation reaches its defined endpoint, allowing for the time-dependent evolution of radiation damage to be modeled in the material.

2.2 Primary Damage and PKA Spectrum

An extensive database of cascades in Ni at various PKA energies ranging from 1 – 10 keV and at temperatures of 300, 425, and 525 K was generated using MD [10] and served as the source of primary defect production due to displacement cascades. The approach accurately captures the size and spatial distribution of defects produced by these cascades. While the average number of Frenkel pairs changes minimally with temperature, defect clustering does change with temperature [10, 14]. Therefore, the OKMC simulations were also conducted at the same temperatures as the MD cascades. Cascades are sampled from the database based on the PKA spectrum of a reactor. The neutron flux for HFIR is approximately 10^5 times higher than that for the PWR. However, for neutron energies greater than 0.1 MeV, the neutron energy spectra for both reactors have similar shapes (see fig. 1 in Ref. [15]). Accordingly, we expect the normalized PKA spectra for both reactors to be identical. Consequently, we used HFIR's PKA recoil spectrum as shown in Fig. 4 from Ref. [15] to conduct the present simulations. In Fig. 4, the probability density measures the number of PKAs (recoils) per unit of energy, and cascades are sampled from the database on the normalized probability density.

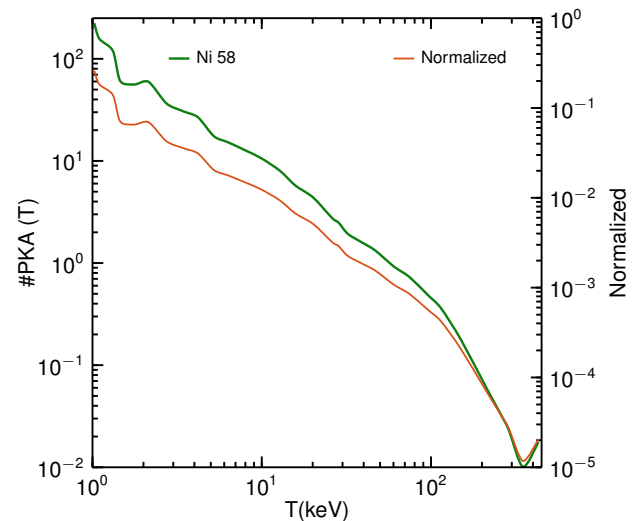


Figure 4: PKA spectra (N° of recoils per unit energy) Vs. the recoil atoms' energy T in pure ^{58}Ni (green) and normalized probability density (spectral density) of a PKA Vs. recoil energy (red)

Based on the PKA spectrum, a cascade is selected randomly from this database and inserted into the simulation cell at random positions based on the cascade production rate, which is the number of cascades inserted into the simulation cell per second, corresponding to a particular dose rate. The production rate of cascades and the accumulated damage, measured as DPA (displacements per atom), are calculated based on the NRT displacements per cascade ν_{NRT} [16]

$$\nu_{NRT} = 0.8 \frac{E_{PKA}}{2E_{th}} \quad (1)$$

where E_{th} is the threshold displacement energy, which is 28 eV for Ni. Note that the cascade production rate depends on the dose rate, average ν_{NRT} per cascade for the PKA spectrum and the number of atoms in the simulation cell (N_{at}). Simulations in the present study were carried out at a dose rate of 1.2×10^{-7} dpa/s, and the corresponding cascade production rate is 0.3333 cascades/s. Simulations were carried up to a dose of 0.3 dpa.

2.3 Simulation Cell

Simulations were conducted using a non-cubic box with dimensions 105.6 nm \times 107.01 nm \times 107.71 nm (i.e., $300a_0 \times 304a_0 \times 306a_0$, where $a_0 = 0.352$ nm is the Ni lattice constant), and with axes parallel to the $\langle 100 \rangle$ crystal directions of the FCC crystal. Since the simulation cell volume is much smaller than the grain size, it is assumed to be at the center of a spherical grain. The grain size effect is incorporated using finite periodic boundary conditions [17, 18]. That is, periodic boundary conditions are applied when a defect crosses a simulation box boundary; however, the defect is removed from the simulation when its displacement measured from its creation is greater than or equal to the grain radius, set at approximately 2.22 μ m. The application of finite boundary conditions is achieved by tracking both the unfolded and folded coordinates of a defect cluster. It is important to note that depending on the dose rate, only the 1D diffusing SIA clusters diffuse fast enough to reach grain boundaries in the time interval between two cascade creation events, assuming their path is not obstructed by other defects, impurities or dislocations. Thus, the initial state of the simulation cell represents a pristine nickel matrix devoid of intragranular defects and distant from any grain boundary.

2.4 Diffusion & Reactions of Defects

Kinetic parameters such as the activation energy barrier for the diffusion of vacancy & SIA clusters, H and the binding energy between them used in the present simulations were collected from the published literature [19–36]. All defects that diffuse in 3D hop along FCC 12 nearest-neighbor directions, while those that diffuse in 1D along six 1D directions along $[110]$ directions

2.4.1 Diffusion & Reaction of Vacancy Clusters

Table 1 shows the activation energy barrier, binding energies and detrapping barriers for vacancy clusters of size 1 to 6. Clusters larger size 6 are considered immobile and stable against dissociation. All vacancy clusters are assumed to have spherical symmetry. The capture radius which is a function of number of vacancies is given as

$$r_{V_n} = r_0 + \left(\frac{3}{16\pi} \right)^{\frac{1}{3}} \left(n^{\frac{1}{3}} - 1 \right) a_0 \quad (2)$$

where a_0 is the lattice constant, n is the number of vacancies in a cluster. and $r_0 = a_0/2\sqrt{2}$, which half the nearest neighbor distance in a FCC lattice. For simplicity, in the present simulations, no distinction is made between voids and stacking fault tetrahedra. It can be seen from Table 1 that activation energy for mono and

Table 1: Activation energy barriers (E_a), binding energies (E_b) and detrapping barriers (E_d) of vacancy clusters. E_d is a sum of binding energy and activation energy barrier for single vacancy. D_0 is the diffusion prefactor.

Size	E_a (eV)	D_0 ($/10^{12}$) (/s)	E_b (eV)	E_d (eV)
1	0.9	56.5		–
2	0.649	6.62	0.2	1.01
3	0.702	6.62	0.38	1.28
4	1.351	6.62	0.54	1.44
5	1.366	6.62	1.1	2.0
6	1.771	6.62	1.376	2.28
$V_n(n > 6)$	5	0		

di-vacancy is quite high and immobile at 300 K. Furthermore, in Ni, di-vacancy diffuses faster than a mono-vacancy and small vacancy clusters are unstable.

2.4.2 Diffusion & Reaction of SIA Clusters

Table 2 shows the activation energies and prefactors for SIA cluster diffusion. SIA clusters of size 1 to 8 diffuse in 3D while clusters of size 9 and larger diffuse in 1D. Furthermore, 1D diffusing SIA clusters were not allowed to change the direction of their 1D paths. Furthermore, all SIA clusters were also assumed to have spherical symmetry with a capture radius that 1.15 times that of a vacancy cluster of equal size. Indicating a longer interaction range of SIA clusters.

Table 2: Activation energies and the corresponding prefactors for SIA cluster diffusion

Size	D_0 ($/10^{12}$) (/s)	E_a (eV)	Dimensionality
1	6.6	0.32	3D
2	6.6	0.55	3D
3	6.6	0.24	3D
4	6.6	0.47	3D
5	6.6	0.72	3D
6	6.6	1.07	3D
7	6.6	1.31	3D
8	6.6	1.58	3D
$9 \leq n \leq 60$	$0.551 + 1.37/n^{1.7}$	$-0.0206 + 0.00518 \times n$	1D

2.4.3 Diffusion of H and He in Ni

2.4.3.1 Helium

Table 3 shows the activation energy barriers and prefactors for He cluster diffusion in Ni from sizes 1 to 6 used in the present simulations. He clusters of size 7 and larger are immobile. Furthermore, He clusters can also undergo trap mutation, which involves ejecting a lattice atom to create a HeV-type defect ($\text{He}_n \rightarrow \text{He}_n\text{V}_1$),

also known as a *He bubble*. All He clusters of size 7 and larger are considered to trap and mutate with zero activation energy barrier. Additionally, as the number of He atoms increase in a bubble, it can kick out additional lattice atoms to create more vacancies. In the present simulations He/V ratio is taken as the criterion for He bubble to kick out additional lattice atoms.

Table 3: Activation energies and the corresponding prefactors for He cluster diffusion

Size	E_a (eV)	D_0 ($/10^{12}$) (/s)	E_b (eV)
1	0.104 ± 0.014	35.28	–
2	0.104 ± 0.014	17.52	0.17
3	0.051 ± 0.006	0.397	0.21
4	0.042 ± 0.003	0.234	0.49
5	0.092 ± 0.013	0.121	0.77
6	0.113 ± 0.001	0.277	0.80

It can be seen from Table 3 that small He clusters are highly mobile and diffuse faster than small SIA clusters. Furthermore, it is important to note that the binding energy of the He₂ cluster is low, allowing it to dissociate even at room temperature.

The capture radius of an interstitial He clusters as a function of its size (n) is given as [37]

$$r_{He_n} = r_1 + \left(\frac{3}{4\pi} \frac{a_0^3}{10} n \right)^{1/3} - \left(\frac{3}{4\pi} \frac{a_0^3}{10} \right)^{1/3} \quad (3)$$

where $r_1 = 3 \text{ \AA}$, a_0 is the lattice constant, n is the number of He atoms in a cluster. In the case of He bubbles, the capture radius is based on the number of vacancies in the defect complex and is given by Eq. (2).

2.4.3.2 Hydrogen

The activation energy barrier for the interstitial is taken as 0.476 eV, with a corresponding prefactor of $6.6 \times 10^{13}/s$. Furthermore, the binding energy between two interstitial H atoms is repulsive, and hence the interstitial H clusters are considered to be unstable. Accordingly, the formation of interstitial H clusters via nucleation is not allowed. Those that form due to the annihilation of vacancies (SIAs) in HeV(HeI)-type clusters dissociate immediately into individual interstitial He atoms. For simplicity, the capture radius of an interstitial H-atom is taken to be the same (Eq. (3)) as an interstitial He-atom.

2.4.4 H and He and their interaction with SIAs and Vacancies

2.4.4.1 Hydrogen

H is known to bind with a vacancy with a binding energy of approximately 0.51 eV. A single vacancy can accommodate a maximum of 6 H atoms, termed a *fully H-loaded* vacancy or vacancy cluster. However, a divacancy can hold up to 4 times that of a mono-vacancy. Accordingly, a *fully H-loaded* vacancy or vacancy clusters, such as H₆V or H₂₄V₂ cluster, respectively, cannot interact with interstitial H-atoms. However, *fully H-loaded* vacancy clusters can still interact with SIAs and vacancies.

Table 4 shows the activation energies and the corresponding prefactors for H_{*n*}V ($1 \leq n \leq 4$) taken from Ref. [28]. Otherwise, all HV-type clusters are considered to be immobile and stable against dissociation. Furthermore, all H-SIA-type clusters were also considered to be immobile. There was only one previous studies

Table 4: Activation energies and the corresponding prefactors H_nV cluster diffusion diffusion

Cluster	D_0 ($/10^{12}$) (/s)	E_a (eV)
HV	17.52	1.13
H ₂ V	0.807	1.17
H ₃ V	0.888	1.29
H ₄ V	0.888	1.4

to mention the interaction between a H atom and a mono-SIA has a negligible binding energy [27]. However, no information is available in the published literature on their stability as a function of SIA cluster size or the interaction of SIA cluster with multiple H atoms. Hence, in the present simulations, all H-SIA type clusters are assumed to be unstable and dissociate immediately.

2.4.4.2 Helium

According to our current knowledge, there are no studies indicating the diffusion of He bubbles in nickel. Therefore, we assumed that He bubbles (or He_nV_m type complexes) are immobile and stable against dissociation. However, they are capable of reacting with other types of defects. It's worth noting that these bubbles can expel a lattice atom, resulting in the creation of a self-interstitial atom (SIA) and an increase in the number of vacancies within the bubble. This reaction can be described by the chemical equation $He_nV_m \longrightarrow He_nV_{m+1} + I_1$. In our current simulations, we have used a He to vacancy ratio (He/V) of 4 as the condition for this reaction to occur, which is the same assumption made in Ref. [26]. Nevertheless, there are no studies in Ni to confirm this.

Table 5: Detrapping barrier and prefactors used for the dissociation of HeI, He₂I and HeI₂ clusters

Cluster	D_0 ($/10^{12}$) (/s)	E_a (eV)
HeI	1.00	1.13
He ₂ I	1.00	0.197
HeI ₂	1.00	0.193

With regards to the interactions between SIA and He clusters, unfortunately, there are no studies on their interactions. This lack of data also extends to the energetics of He-SIA-type clusters. Therefore, we conducted a limited number of static MD studies to compute the detrapping energy barriers for He atoms from small He-SIA type defect-complexes, with their values presented in Table 5. Additionally, we found that He-SIA-type complexes appear to be immobile. Nevertheless, it is important to note that a comprehensive study of the interactions between He and H with SIA clusters is required.

3.0 Results and Discussions

To understand the influence of hydrogen (H) and helium (He) on the accumulation of irradiation damage in pure nickel, we conducted three sets of simulations:

- No production of gaseous transmutants
- With the H production due to transmutation or other sources
- With the He production due to transmutation.

3.1 Without H and He

As mentioned earlier, these simulations have no extended defects, such as dislocations, intragranular impurities, or traps. The simulations were carried out at temperatures 300, 425, and 525 K, aligning with the temperatures at which the cascades were generated. The dose rate used was 1.2×10^{-7} dpa/s, comparable to the dose rate nickel would experience in a PWR. More importantly, with increasing dose, the densities saturate at 425 and 525 K, while at 300 K, they show a non-zero slope, albeit decreasing, suggesting a potential further increase in densities.

Figures 5 to 7 shows the volumetric densities of vacancies and vacancy clusters, as well as the average size of vacancy clusters, measured by the number of vacancies at 300, 425, and 525 K without H and He production. The densities of vacancies and vacancy clusters are observed to decrease, while the average size of the clusters increases with temperature. Additionally, the dose at which the vacancy cluster density saturates decreases with increasing temperature. Although the average size of vacancy clusters generally seems to increase with dose, the increase rate tends to slow down at higher temperatures.

At 300 K, only SIA clusters are mobile, with those capable of 1D diffusion being highly mobile (see Table 2). However, the production of SIA clusters of size 7 and larger from displacement cascades is minimal [10], resulting in a predominance of 3D diffusing SIA clusters. Although there is a slight increase in SIA clustering with increasing temperature and PKA energy [10], the vast majority of SIA clusters remain smaller than size 7 thus diffuse in 3D. Conversely, all vacancy clusters diffuse in 3D, with di-vacancy clusters being more mobile than mono-vacancy clusters (see

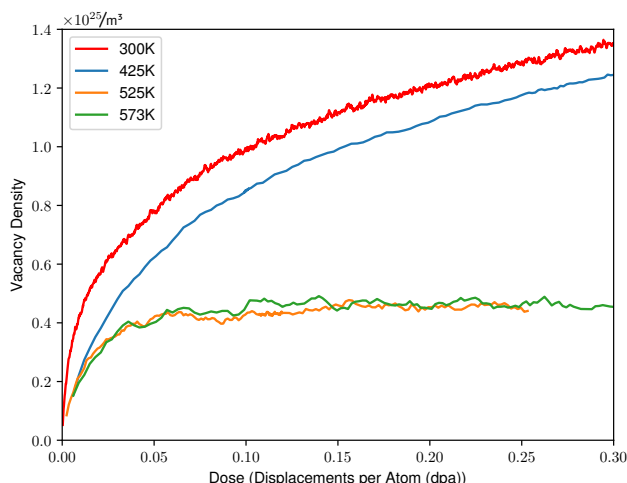


Figure 5: Density of vacancies

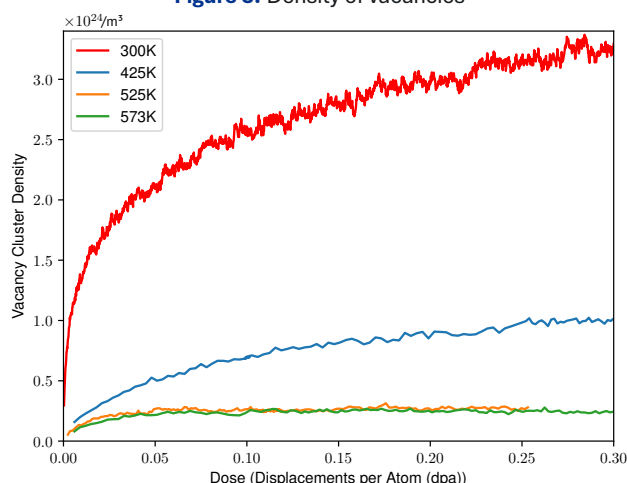


Figure 6: Density of Vacancy clusters

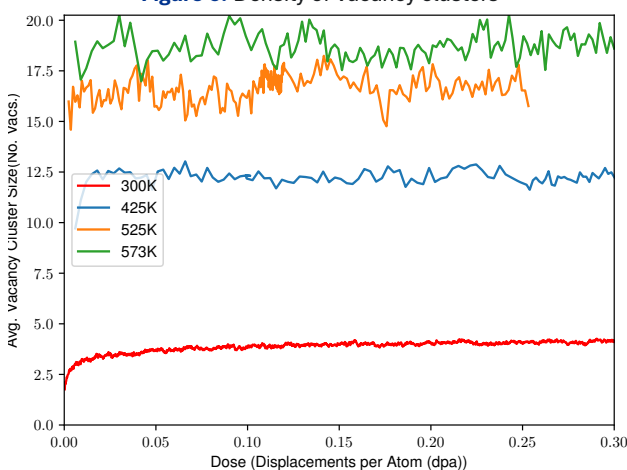


Figure 7: Average vacancy cluster sizes (N^0 of vacancies)

Table 1), and the mobility drops significantly with increasing cluster size. Additionally, small vacancy clusters tend to be unstable at higher temperatures due to their significantly lower binding energies than SIA clusters. Furthermore, the in-cascade clustering of vacancies is minimal [10].

At 300 K, only small SIA clusters, mainly mono- and tri-SIA clusters, exhibit slow diffusion. However, as the temperature rises, the mobility of all 3D diffusing SIA clusters also increases, leading to higher concentrations of mobile SIA clusters. As temperatures increase, it results in higher recombination rates and a lower vacancy concentration, as illustrated in Fig. 5. In the case of vacancy clusters, with increasing temperature, not only does the mobility of vacancy clusters increase, but the rate of dissociation of small vacancy clusters also increases, releasing mono-vacancies. These mobile vacancies are then captured by larger, more stable vacancy clusters, leading to a decrease in vacancy cluster density and an increase in their average size with increasing temperature, as shown in Figs. 6 and 7. Therefore, it is easy to see that the diffusion and dissociation of vacancy clusters determine the density and size of vacancy clusters.

As the density of vacancy clusters increases with dose, the probability that previously formed vacancy clusters capture the mobile vacancies increases rather than contributing to the nucleation of new clusters. Consequently, the rate of increase of vacancy cluster density is expected to decrease with increasing dose, ultimately reaching saturation at a certain dose level (refer to Fig. 6). However, with increasing temperature, the distances small vacancy clusters can travel within the time gap between successive cascade creation and the critical size to nucleate new vacancy clusters increases. Thus, with increasing temperature, the overall density of vacancy clusters decreases while the average size of these clusters increases (see Figs. 6 and 7).

3.2 With H

Simulations incorporating H production were conducted at rates of 0.05 and 1.0 H atoms per second, using the same parameters as those in the simulations without H production. These simulations began with zero H concentration, and H atoms were randomly inserted into the simulation box at the specified production rate. We found that the behavior of damage accumulation with increasing dose was similar at both rates. Therefore, for brevity, we only show the plots for the rate of 0.05 H atoms per second. Nevertheless, we will briefly discuss the influence of the H production rate.

Figures 8 to 10 display the *total* density of vacancies and vacancy clusters, along with the average size of these clusters. The total density of vacancies encompasses those within *pure* vacancy clusters as well as HV-type clusters. Consequently, the *total* vacancy cluster density is the aggregate of densities from *pure* vacancy clusters and HV-type clusters. Similarly, the average total vacancy cluster size represents the average number of vacancies per cluster, whether in pure or HV-type clusters. The Figs. 11 to 13 display the densities and average size for vacancies in *pure* vacancy clusters.

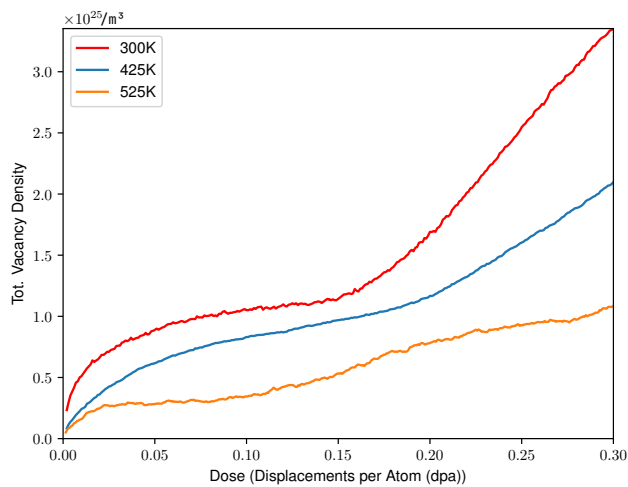


Figure 8: Total density of vacancies

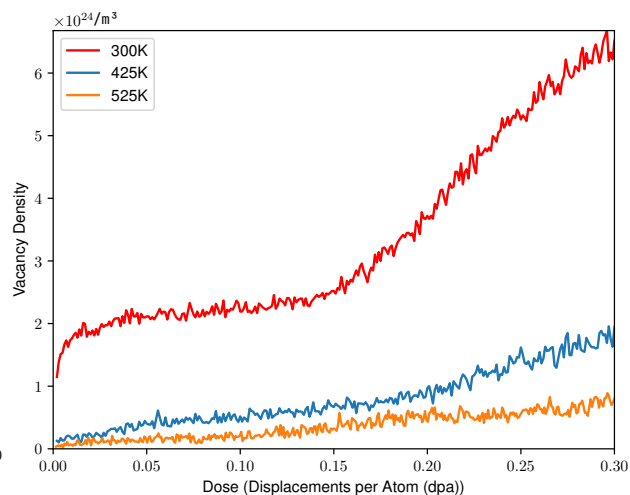


Figure 11: Vacancy density in pure vacancy clusters

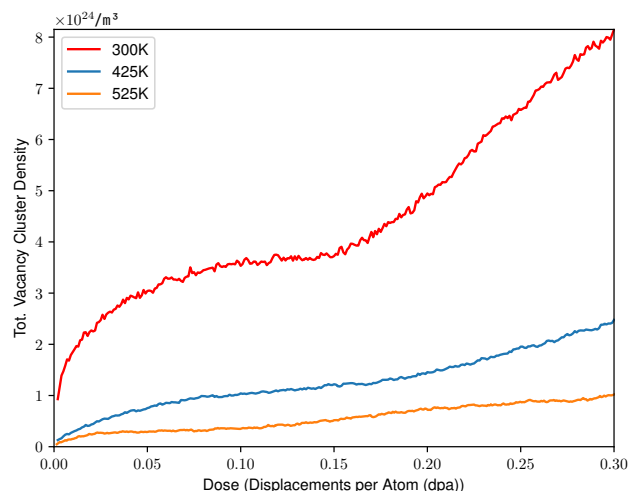


Figure 9: Total density V and HV clusters

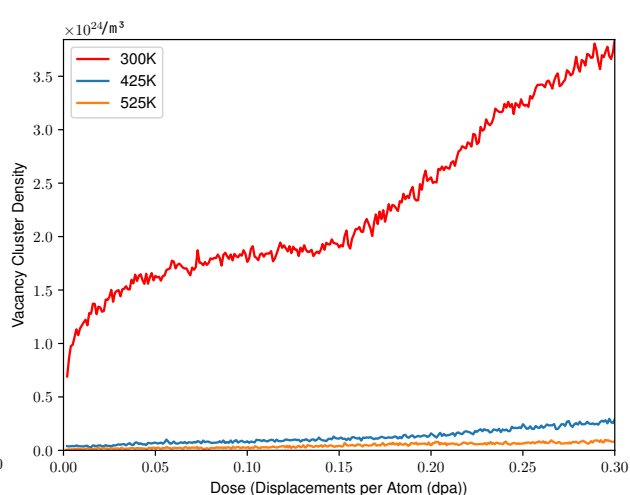


Figure 12: Pure vacancy cluster density

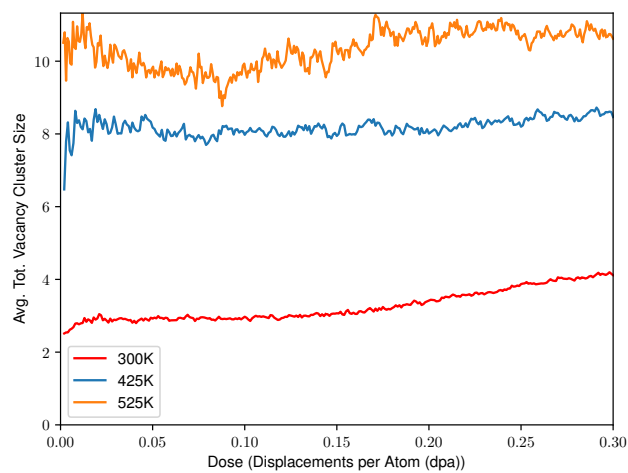


Figure 10: Combined average N^0 of vacancies in V and HV

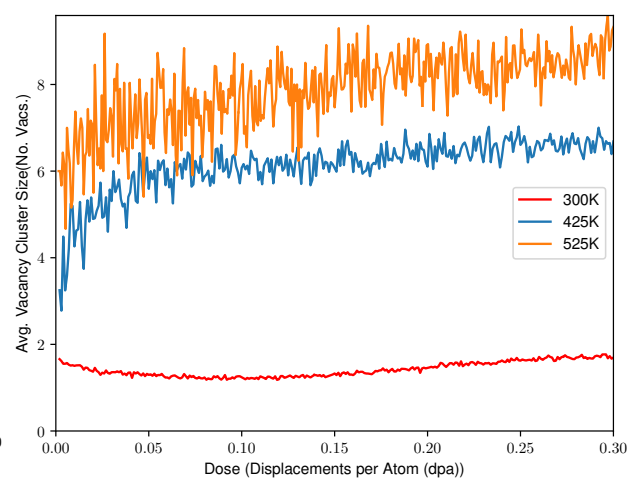


Figure 13: Average N^0 of vacancies per cluster

From Figs. 8 to 13, it is evident that the presence of H significantly influences damage accumulation and its evolution with dose compared to scenarios without H production. As shown in Figs. 8 and 9, across all three temperatures (300 K, 425 K, and 525 K), the total densities of vacancies and vacancy clusters first reach saturation, then increase again as the dose increases. This trend is particularly pronounced for vacancy and vacancy cluster densities at 300 K, whereas at 425 K and 525 K, it is more observable in the vacancy density than in the vacancy cluster density. Conversely, a similar saturation and subsequent increase are noted in the pure vacancy cluster cases at 300 K. However, at 425 K and 525 K, the densities of pure vacancy clusters and the vacancies within them appear to increase linearly with dose escalation. Regarding the total average vacancy cluster size, a trough is observed at lower doses, indicating a decrease in average size, which becomes less pronounced and narrower with increasing temperature, especially noticeable at 525 K (see Fig. 10). The trough indicates the stabilization of small vacancy clusters by the presence of H. Beyond the trough, the average vacancy cluster size increases with dose at 300 and 525 K; however, it is hard to discern at 425 K (see Fig. 10). In the case of pure vacancy cluster size, similar behavior is observed only at 300 K. Since at 300 K, both V_n and He_nV_1 cluster are immobile, an increase in size above 0.15 dpa suggest coalescence of small clusters. While at 525 K, it is likely due to the diffusion of V_n and He_nV_1 . A thorough data analysis of diffusion and reaction events as a function of dose and temperature is required to discern the effect of H fully.

Nonetheless, it is evident from Figs. 8 to 13 that the effect of temperature on damage accumulation mirrors that observed without H production. Specifically, the densities of vacancies and vacancy clusters decrease, whereas the average size increases. Furthermore, the stabilization of vacancy clusters due to H is reflected by an increase in density and a decrease in the average size. Increasing the H-production rate to 1.0 H-atoms per second intensifies the effects at 0.05 H-atoms per second. Notably, based on the present understanding of defect-defect interactions in Ni, our simulations suggest that in the initial stages of irradiation, H does not promote void growth but enhances the stability of small vacancy clusters, thereby facilitating void nucleation

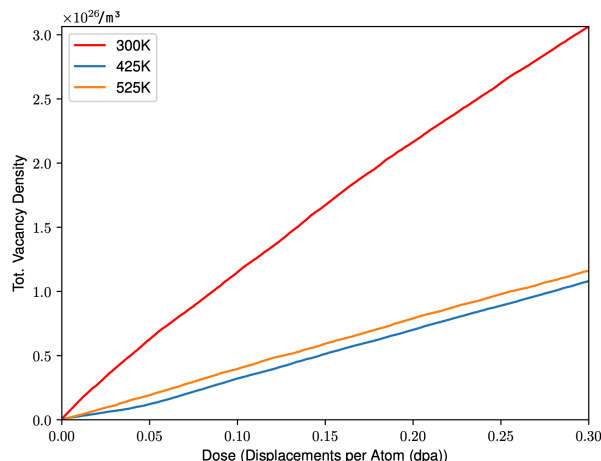


Figure 14: Total density of vacancies

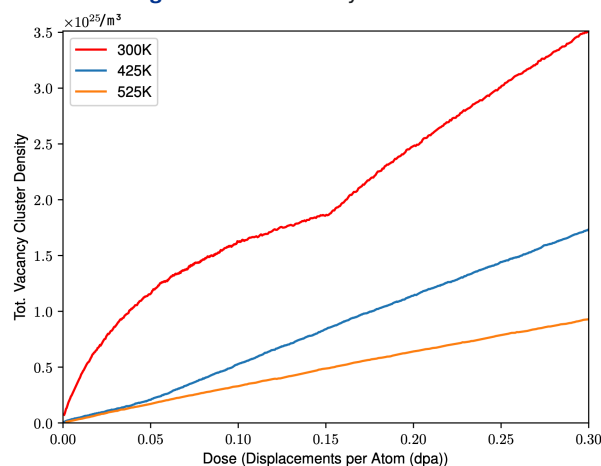


Figure 15: Total density V and HeV clusters

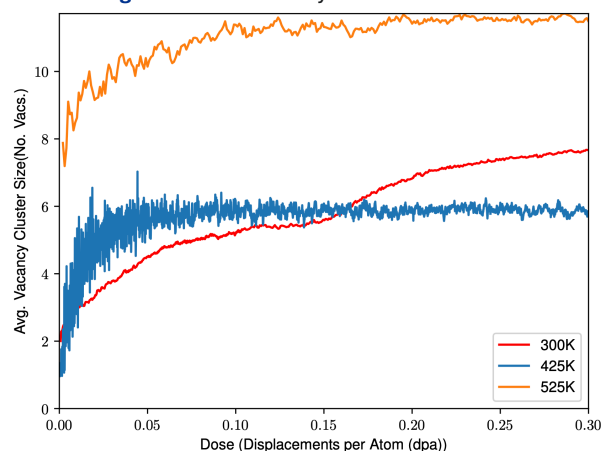


Figure 16: Combined average N^0 vacancies in V and HeV

3.3 With He

Simulations incorporating He production were performed at 0.05 He atoms per second, maintaining the same parameters as the simulations without He production. These simulations started with zero He concentration, with He atoms are randomly created in the simulation box at the set production rate. Figures 14 to 16 display the *total* density of vacancies and vacancy clusters, alongside the average size of these clusters. The total density of vacancies includes those in *pure* vacancy clusters and in HeV-type clusters, leading to a *total* vacancy cluster density that combines the densities from *pure* vacancy clusters and HeV-type clusters. The average total vacancy cluster size reflects the average number of vacancies per cluster, whether they are in pure or HeV-type clusters.

The influence of temperature on damage accumulation remains consistent when considering scenarios with and without H production, as well as with He production. Although there are differences in how damage accumulation progresses with dose in the presence of H and He, the overall impact of both H and He production is similar. In both cases, the densities of vacancies and vacancy clusters are higher, while the average size of these clusters is reduced compared to scenarios without H and He. This suggests that even with He, its presence during the initial stages of irradiation does not appear to enhance void growth, but rather enhances the nucleation of voids. However, the higher diffusivity of helium, its stronger binding with vacancy clusters, and its ability to displace a nearby lattice atom could result in a larger average vacancy cluster size, as evidenced by comparing Figs. 10 and 16. Therefore, it is likely that void growth will occur after the nucleation phase, especially as more He accumulates at higher doses than those simulated in this study.

4.0 Summary

In this study, we executed OKMC simulations of irradiation damage in nickel under Pressurized Water Reactor (PWR) conditions at 300, 425, and 525 K, considering scenarios with and without the production of H and He. The aim was to clarify the TEM-observed discrepancies in void microstructure between the inner and outer nickel coatings of the zircaloy-4 getter tubes in Tritium Producing Burnable Absorber Rods (TPBARs). Notably, voids in the inner coating were three times larger than those in the outer coating, although both exhibited similar void densities. We hypothesized that differences in the fluxes of ^3H and/or He between the coatings might explain these microstructural variations. Our simulations incorporated current knowledge on the energetics of diffusion of H and He and their reactions with irradiation-induced point defects. Considering that our models represent an idealized nickel sample free from intragranular impurities and extended defects and far from grain boundaries, we do not anticipate quantitative alignment with experimental results. However, a qualitative correspondence would offer valuable insights into the fundamental mechanisms governing microstructural evolution during irradiation.

The influence of temperature on damage accumulation and its variation with dose observed in our simulations qualitatively aligns with experimental observations. Specifically, the density of vacancy clusters decreases while their average size increases with temperature. This behavior persists in simulations involving H and He production, suggesting that such qualitative trends are likely independent of the initial microstructure. Additionally, in the absence of H and He production the dose at which the vacancy cluster density reaches saturation diminishes as the temperature rises.

Although there are noticeable differences in the dynamics of damage accumulation between scenarios with hydrogen and helium production, both show an increase in vacancy cluster density and a reduction in average cluster size. Furthermore, an increase in the rate of hydrogen production intensifies these effects, indicating that the presence of hydrogen and helium during the initial stages of irradiation primarily promotes the formation of vacancy clusters (voids) by stabilizing smaller clusters against thermal dissociation rather than promoting void growth.

Unfortunately, there are no experimental studies in the literature to confirm the behavior of void densities with increasing doses in the presence of hydrogen or helium. However, in a study by Garner *et al.* [38], the authors found an increase in the density of voids and bubbles due to hydrogen retention in neutron-irradiated FCC metals. In another study by Jia *et al.* [39], the authors found large and isolated cavities formed under single ion Ni^+ irradiation of Ni. However, triple ions (Ni^+ , He^+ and H^+) induced smaller and denser cavities and higher swelling. On the other hand, helium's higher diffusivity, stronger binding with vacancy clusters, and ability to displace a nearby lattice atom could result in a larger average vacancy cluster size. Therefore, it is likely that void growth will occur after the nucleation phase as more helium accumulates at higher doses than those simulated in this study.

Our simulations integrate nearly all available numerical data and current understanding of the reaction-diffusion mechanisms of various defect types, and hence are the most realistic models of irradiation damage possible with present knowledge. Qualitatively, our results suggest that a higher hydrogen (H) production rate should lead to smaller void sizes. However, a higher H rate is expected in the inner coating, raising the question of why voids are larger there than in the outer coating.

Our results also reveal gaps in the current understanding of defect-defect interactions in the presence of hydrogen (H) and helium (He), especially regarding interactions between interstitial H and He, as well as H-vacancy (HV) and He-vacancy (HeV) with Self-Interstitial Atom (SIA) clusters. Our simulations assume that vacancies in HV and HeV-type clusters will inevitably recombine with SIAs. However, evidence from the scientific literature [40–44] in other metals suggests that strong binding between an impurity and a vacancy

may inhibit this recombination. Moreover, the immediate formation of HeV-SIA defect complexes following trap mutation, where the newly created SIA remains temporarily attached to the He bubble, indicates that the presence of He could hinder recombination. Given that both H and He are produced simultaneously under irradiation conditions, a deeper understanding of their synergistic effects in nickel is essential. This gap highlights the need for further studies to clarify these interactions and their impact on irradiation damage accumulation.

5.0 References

- [1] K. A. Burns, E. F. Love, C. K. Thornhill, *Description Of The Tritium-Producing Burnable Absorber Rod For The Commercial Light Water Reactor*, TQP-1-015, Rev 19 PNNL-22086, February, 2012.
- [2] D. J. Senior, *Recommendations for Tritium Science and Technology Research and Development in Support of the Tritium Readiness Campaign*, TTP-7-084, PNNL-22873, October, 2013.
- [3] L. R. Greenwood, F. A. Garner, *Hydrogen generation arising from the $^{59}\text{Ni}(n, p)$ reaction and its impact on fission—fusion correlations* *J. Nucl. Mater.* **233**, 1530–1534 (1996).
- [4] D. J. Edwards, M. Olszta, D. Sunderland, A. Devaraj, A. Schemer-Kohn, B. Matthews, *PIE of Cycle 13316 SS Cladding and Getter Tube from Mid Plane Region*, Tritium Science Meeting, September 10, 2021.
- [5] G. Nandipati, *Kinetic Simulations of Microstructural Evolution (KSOME)*, software (2020).
URL <https://www.osti.gov/doecode/biblio/42010>
- [6] G. Nandipati, W. Setyawan, H. L. Heinisch, K. J. Roche, R. J. Kurtz, B. D. Wirth, *Object Kinetic Monte Carlo Simulations of Microstructure Evolution*, Semiannual Progress Report DOE/ER-0313/54 (June 2013) 179–183.
- [7] G. Nandipati, W. Setyawan, H. L. Heinisch, K. J. Roche, R. J. Kurtz, B. D. Wirth, *Displacement cascades and defect annealing in tungsten, Part II: Objectkinetic Monte Carlo simulation of tungsten cascade aging* *J. Nucl. Mater.* **462** (2015) 338–344.
- [8] G. Nandipati, W. Setyawan, K. J. Roche, R. J. Kurtz, B. D. Wirth, *Effect of Confinement of SIA Cluster Diffusion by Impurities on Radiation Defect Accumulation due to 14 MeV Neutrons in Tungsten* *J. Nucl. Mater.* **542** (2020) 152402.
- [9] G. Nandipati, K. D. Hammond, D. Maroudas, K. J. Roche, R. J. Kurtz, B. D. Wirth, W. Setyawan, *Effect of Helium Flux on Near-surface Helium Accumulation in Plasma-exposed Tungsten* *J. Phys: Condens. Mater.* (2022) **34** 035701.
- [10] M. Fullarton, G. Nandipati, D. J. Senior, A. M. Casella, R. Devanathan, *Molecular Dynamics Study of Primary Damage in the Near-Surface Region in Nickel* *J. Nucl. Mater.* **583** (2023) 154514.
- [11] H. L. Heinisch, *Defect Production in Simulated Cascades: Cascade Quenching and Short-term Annealing* *J. Nucl. Mater.* **117** (1983) 46–54.
- [12] A. Bortz, M. H. Kalos, J. L. Lebowitz, *A New Algorithm For Monte Carlo Simulation of Ising Spin Systems* *J. Comput. Phys.* **17** (1975) 10–18.
- [13] L. J. Blue, I. Beichl, F. Sullivan, *Faster Monte Carlo Simulations* *Phys. Rev.* **E51** (1995) R867–R868.
- [14] A. Chaka, M. Efe, S. Kulkarni, G. Nandipati, R. Devanathan, *Getter performance modeling*, Tech. rep., Pacific Northwest National Laboratory (PNNL-30584, October 2020).
- [15] L. Luneville, J. C. Sublet, D. Simeone, *Impact of Nuclear Transmutations on the Primary Damage Production: The Example of Ni Based Steels* *J. Nucl. Mater.* **505** (2018) 262–266.
- [16] M. Norgett, M. Robinson, I. Torrens, *A Proposed Method of Calculating Displacement Dose Rates* *Nucl. Eng. Des.* **33** (1975) 50–54.
- [17] H. L. Heinisch, B. N. Singh, *The effects of one-dimensional migration of self-interstitial clusters on the formation of void lattices*, *J. Nucl. Mater.* (2002) **307–311** 876–880.
- [18] N. Soneda, S. Ishino, A. Takahashi, K. Sohi, *J. Nucl. Mater.* (2003) **323** 169–180.
- [19] S. Mahmoud, M. Trochet, O. A. Restrepo, N. Mousseau, *Study Of Point Defects Diffusion In Nickel Using Kinetic Activation-Relaxation Technique* *Acta Mater.* **144**, 679–690 (2018).
- [20] D. S. Aidhy, C. Lu, K. Jin, H. Bei, Y. Zhang, L. Wang, W. J. Weber, *Formation And Growth Of Stacking Fault Tetrahedra In Ni Via Vacancy Aggregation Mechanism* *Scripta Mater.* **114**, 137–141.

- [21] J. Tucker, R. Najafabadi, T. Allen, D. Morgan, *Ab Initio-Based Diffusion Theory And Tracer Diffusion In Ni–Cr And Ni–Fe Alloys* *J. Nucl. Mater.* **405**, 216–234 (2010).
- [22] B. Gámez, L. Gámez, C. Ortiz, M. Caturla, J. Perlado, *Object Kinetic Monte Carlo Calculations Of Electron And He Irradiation Of Nickel* *J. Nucl. Mater.* **386–388**, 90–92 (2009).
- [23] S. Zhao, Y. Zhang, W. J. Weber, *Stability Of Vacancy-Type Defect Clusters In Ni Based On First-Principles And Molecular Dynamics Simulations* *Scripta Mater.* **145**, 71–75 (2018).
- [24] Y. Osetsky, A. Barashev, Y. Zhang, *On The Mobility Of Defect Clusters And Their Effect On Microstructure Evolution In FCC Ni Under Irradiation* *Materialia* **4**, 139–146 (2018).
- [25] P. Zhao, Y. Shimomura, *Molecular Dynamics Calculations of Properties of the Self-interstitials in Copper and Nickel* *Comput. Mater. Sci.* **14**, 84–90 (1999).
- [26] K. Ferasat, I. Martin-Bragado, Z. Yao, L. K. Béland, *He bubble Growth in Nickel Simulated by Object Kinetic Monte Carlo* *J. Nucl. Mater.* **576** 154231 (2023).
- [27] D. Connetable, Y. Wang, D. Tanguy, *Segregation Of Hydrogen To Defects In Nickel Using First-Principles Calculations: The Case Of Self-Interstitials And Cavities* *J. Alloys Compd.* **614**, 211–220 (2014).
- [28] Y. Wang, D. Connétable, D. Tanguy, *Hydrogen Influence On Diffusion In Nickel From First-Principles Calculations* *Phys. Rev. B* **91**, 094106 (2015).
- [29] D. J. Hepburn, D. Ferguson, S. Gardner, G. J. Ackland, *First-Principles Study Of Helium, Carbon, And Nitrogen In Austenite, Dilute Austenitic Iron Alloys, And Nickel* *Phys. Rev. B* **88**, 024115 (2013).
- [30] E. Torres, J. Pencer, D. Radford, *Atomistic Simulation Study Of The Hydrogen Diffusion In Nickel* *Comput. Mater. Sci.* **152**, 374–380 (2018).
- [31] D. Connétable, E. Andrieu, D. Monceau, *First-Principles Nickel Database: Energetics Of Impurities And Defects* *Comput. Mater. Sci.* **101**, 77–87 (2015).
- [32] M. David, A. Prillieux, D. Monceau, D. Connetable, *First-Principles Study Of The Insertion And Diffusion Of Interstitial Atoms (H, C, N And O) In Nickel* *J. Alloys Compd.* **822**, 153555 (2020).
- [33] A. V. Subashiev, H. H. Nee, *Hydrogen Trapping At Divacancies And Impurity-Vacancy Complexes In Nickel: First Principles Study* *J. Nucl. Mater.* **487**, 135–142 (2017).
- [34] W. Xing, X.-Q. Chen, X. Li, Y. Ma, B. Chen, K. Liu, *First-Principles Study Of Hydrogen Trapping Behavior In Face Centered Cubic Metals (M=Ni, Cu And Al) With Monovacancy* *Int. J. Hydrogen Energy* **45**, 25555–25566 (2020).
- [35] N. K. Das, T. Shoji, T. Nishizumi, T. Fukuoka, T. Sugawara, R. Sasaki, T. Tatsuki, H. Yuya, K. Ito, K. Sakima, K. Tsutsumi, S. Ooki, Y. Sueishi, K. Takeda, *First-Principles Calculations Of Hydrogen Interactions With Nickel Containing A Monovacancy And Divacancies* *Mater. Res. Express* **4**, 076505 (2017).
- [36] G. Nandipati, D. J. Senior, A. M. Casella, A. Soulam, *Molecular dynamics study of interstitial He clusters in nickel* *Nucl. Mater. Energy* **41**, 101733 (2024).
- [37] C. Becquart, C. Domain, U. Sarkar, A. DeBacker, M. Hou, *Microstructural Evolution Of Irradiated Tungsten: Ab Initio Parameterisation Of An OKMC Model* *J. Nucl. Mater.* **403**, 75–88 (2010).
- [38] F. Garner, E. Simonen, B. Oliver, L. Greenwood, M. Grossbeck, W. Wolfer, P. Scott, *Retention of hydrogen in fcc metals irradiated at temperatures leading to high densities of bubbles or voids* *J. Nucl. Mater.* **356**, 122–135 (2006).
- [39] H. Jia, G. Zhiying, L. Haocheng, M. Pengfei, L. Yan, G. Wei, L. Fengping, C. Liuxuan, H. Jinch, X. Jianming, W. Yugang, W. Chenxu, *Effect of Damage Rate on the Cavity Swelling of Pure Nickel Irradiated with Triple Ion Beams* *Metals* **12**, 7 (2017).
- [40] S. Qin, S. Jin, L. Niu, J. Hao, H. Zhou, G. Lu, *The effect of hydrogen on the recombination of Frenkel pair in tungsten: A theoretical insight* *Sci. China– Phys. Mech. Astron.* **60**, 067021 (2017).

- [41] D. Terentyev, N. Anento, A. Serra, V. Jansson, H. Khater, G. Bonny, *Interaction of carbon with vacancy and self-interstitial atom clusters in α -iron studied using metallic–covalent interatomic potential* *J. Nucl. Mater.* **4008**, 272–284 (2011).
- [42] N. Anento, A. Serra, *Carbon–vacancy complexes as traps for self-interstitial clusters in Fe–C alloys* *J. Nucl. Mater.* **440** 236–242 (2013).
- [43] Y. Wei, N. Gao, Z. Shen, C. Chen, Z. Xie, L. Guo, *Interactions between hydrogen bubbles and prismatic interstitial dislocation loops in BCC iron* *Comput. Mater. Sci.* **180**, 109724 (2020).
- [44] H. Hao-Xuan, L. Yu-Hao, L. Zhong-Zhu, H. Peng-Wei, M. Fang-Fei, R. Qing-Yuan, Z. Hong-Bo, L. Guang-Hong, *Role of hydrogen in stability and mobility of vacancy clusters in tungsten* *Tungsten* **4**, 3 (2017).

Pacific Northwest National Laboratory

902 Battelle Boulevard
P.O. Box 999
Richland, WA 99352
1-888-375-PNNL (7675)

www.pnnl.gov